Research Article | Vol. 12, No. 1 / 1 January 2021 / Biomedical Optics Express 539
Biomedical Optics EXPRESS

Uptake quantification of gold nanoparticles inside of cancer cells using high order image correlation spectroscopy

DELARAM KATOOZI, ANDREW H. A. CLAYTON, DAVID J. MOSS, AND JAMES W. M. CHON*

Optical Sciences Centre, Department of Physics and Astronomy, Faculty of Science, Engineering and Technology, Swinburne University of Technology, PO Box 218, Hawthorn 3122, Victoria, Australia
jchon@swin.edu.au

Abstract: The application of gold nanoparticles (AuNPs) in cancer therapeutics and diagnostics has recently reached a clinical level. Functional use of the AuNP in theranostics first requires effective uptake into the cells, but accurate quantification of AuNPs cellular uptake in real-time is still a challenge due to the destructive nature of existing characterization methods. The optical imaging-based quantification method is highly desirable. Here, we propose the use of high-order image correlation spectroscopy (HICS) as an optical imaging-based nanoparticle quantification technique. Coupled with dark field microscopy (DFM), a non-destructive and easy quantification method could be achieved. We demonstrate HICS analysis on 80 nm AuNPs coated with cetyltrimethylammonium bromide (CTAB) uptake in HeLa cells to calculate the percentage of aggregate species (dimer) in the total uptake and their relative scattering quantum yield inside the cells, the details of which are not available with other quantification techniques. The total particle uptake kinetics measured were in a reasonable agreement with the literature.

1. Introduction

AuNPs, due to their variability in shape, size, material hybridization and functionalization, are becoming one of the major agents in cancer therapeutics [1–12], diagnostics [13–17], targeted drug delivery [18–21], cell function regulation [22–26], biolabeling [27–32], and immunology [33]. Virtually all these applications require uptake of nanoparticles into the target cells to realise their designed functionality, hence much research has been devoted to controlling the uptake and accurate quantification of nanoparticles [34–52]. For absolute quantification, characterization methods such as inductively coupled plasma – atomic emission spectroscopy (ICP – AES) [34–36,48,49,51] inductively coupled plasma – mass spectroscopy (ICP-MS) [38,41,52], transmission electron microscopy (TEM) [39], or dark-field microscopy (DFM) [37] are used. Other methods such as two-photon microscopy [38,47], flow cytometry [41,42], confocal laser scanning microscopy (CLSM) [41,45], Raman spectroscopy [50], and hyperspectral dark-field imaging [22,32,50] can only contribute as relative quantification techniques.

Because the absolute quantification methods (ICP-AES, ICP-MS, TEM) are destructive and cannot be used for real-time live-cell imaging, it is desirable to further develop the existing optical imaging methods into one that is capable of measuring uptake quantity. So far, optical imaging methods have been used as intensity integration [37,41,45,47] or spectral integration [22,32] techniques to account for the relative uptake, but these techniques are limited for AuNPs due to plasmon coupling between particles, which may reduce/enhance detected signals leading to a distortion in the estimated overall number of particles. Scattering or luminescence intensity response of aggregates of plasmonic particles is neither proportional, nor functionally defined by the number of particles within [37], which makes accurate quantification extra challenging.

#417321 https://doi.org/10.1364/BOE.417321
Journal © 2021 Received 10 Dec 2020; accepted 14 Dec 2020; published 22 Dec 2020

Biomedical Optics EXPRESS

Previously, image correlation spectroscopy (ICS) was used to optically quantify fluorophore aggregation and overall concentration of biomolecules attached to cell membrane [53–55]. ICS is an imaging extension of fluorescence correlation spectroscopy (FCS), in which spatially correlated fluorescence or scattering image extracts average number of emitters in a focal volume. There are many variant techniques available to ICS, including image cross-correlation spectroscopy (ICCS) [56], spatial-temporal ICS (STICS) [57], photobleaching ICS [58,59] and raster-scan ICS (RICS) [60], which characterize hetero-oligomerization, local diffusion and photobleaching inside live biological environment. However, the estimation of molecular aggregation in ICS requires the assumption that the fluorescence or emission quantum yield must be unaffected by aggregation, which puts limitation on their use in plasmon-coupled AuNPs.

One of the variants of the ICS, High-order ICS (HICS) [61–64] is a technique that does not require such underlying assumption. The technique utilizes the moment analysis of intensity fluctuations in the image to determine aggregate concentration. A unique feature of this technique is that the quantum yield of an aggregate, for example, a dimer, can be varied without affecting the estimation of its concentration. If the dimer emission quantum yield or cross section is known, then this can be used in the analysis to determine the dimer concentration. In an ideal situation there would be no change in quantum yield in the dimer to that of the monomer hence the total emission is simply 2 times that of monomer [63]. However, for a plasmon coupled dimer scattering/absorption cross sections may vary between 2 to 4 times that of a monomer.

Here, we demonstrate the feasibility of using HICS to account CTAB coated 80 nm AuNPs uptake into HeLa cells. We show that HICS can be applied to DFM imaging of the cells with AuNPs, which allows easy, non-destructive quantification of cellular uptake. This technique can be applied at single cellular level, identifying individual uptake characteristics that might have been undetectable in an ensemble averaging techniques. We firstly show a validation of HICS through analysis over computer simulated optical images and set its boundary in accuracy. Secondly, HICS analysis is further validated for DFM images of randomly distributed 80 nm AuNPs on a coverslip glass. These results pave the way for applying HICS on DFM images of HeLa cells with AuNPs to extract the temporal dynamics of nanoparticle uptake by HeLa cells. Good agreement with the literature confirms the validity of the method.

2. Theory

2.1. Theory of HICS

A general spatial autocorrelation $g(\xi, \eta)$ is a function defined as [54],

$$g(\xi,\eta) = \frac{\langle \delta i(x,y)\delta i(x+\xi, y+\eta)\rangle}{\langle i(x,y)\rangle^2}, \tag{1}$$

where $\delta i(x,y)$ is intensity fluctuation of a pixel at x and y of an image, i.e., $i(x,y) - i(x,y)$ with $i(x,y)$ being the pixel intensity at position (x, y), and square bracket $i(x,y)$ representing the pixel intensity average of the entire image. The significance of the spatial autocorrelation function is that average emitter number n_p in a focal volume can be measured by the magnitude of autocorrelation function $g(0,0)$, due to the properties of the Poisson distribution of emitter statistics inside a focal volume.

$$g(0,0) = \lim_{\xi,\eta\to 0} g(\xi,\eta) = \frac{1}{\langle n_p\rangle} \tag{2}$$

If there are more than one aggregate species in the system, then the high-order autocorrelation function can be used to extract the information on aggregates, defined as [61–63]

$$g_{n,m}(\xi,\eta) = \frac{\langle \delta i^n(x,y)\delta i^m(x+\xi, y+\eta)\rangle - \langle \delta i^n(x,y)\rangle \langle \delta i^m(x,y)\rangle}{\langle i(x,y)\rangle^{n+m}}. \tag{3}$$

Biomedical Optics EXPRESS

The values of n and m are positive integers that determine the order of the correlation. Because the contribution from aggregate intensity is higher in $g_{n,m}$ (0,0), it becomes a function of aggregate concentration and one can build up a series of simultaneous equations to solve individual aggregate concentration. The first 6 expressions of the $g_{n,m}$ (0,0) function for a Gaussian focus are shown in Eq. (4) and (5).

$$\begin{aligned} g_{1,1}(0) &= B_2 \\ g_{1,2}(0) &= 4B_3/3 \\ g_{2,2}(0) &= 2B_4 + 2B_2^2 \\ g_{1,3}(0) &= 2B_4 + 3B_2^2 \\ g_{2,3}(0) &= 16B_5/5 + 12B_2B_3 \\ g_{3,3}(0) &= 16B_6/3 + 30B_2B_4 + 15B_2^3 + 16B_3^2 \\ &\vdots \end{aligned} \tag{4}$$

where

$$B_k = \frac{\sum_{i=1}^{R} \alpha_i^k \langle N_i \rangle}{\left(\sum_{i=1}^{R} \alpha_i \langle N_i \rangle \right)^k}, \tag{5}$$

α_i is the quantum yield (or brightness) ratio of ith species to that of a monomer, and N_i is the average number of ith species in the focal volume. R is the total number of species. For example, if there are two species ($R = 2$) and α_2 is known (i.e., quantum yield ratio of dimer to monomer) then $g_{1,1}$ (0,0) and $g_{1,2}$ (0,0) can be simultaneously solved to extract average monomer and dimer concentrations in a focal volume (N_1 and N_2, respectively). Alternatively, if α_2 is unknown, then $g_{1,3}$ (0,0) or $g_{2,2}$ (0,0) can be further calculated from the image, meaning that there are three simultaneous equations to solve for three unknowns (N_1, α_2 and N_2). These are shown in Eq. (6). This can be further extended to higher order equations if there are more unknown species concentrations [22,26].

$$\begin{aligned} B_2 &= \frac{\langle N_1 \rangle + \alpha_2^2 \langle N_2 \rangle}{\left(\langle N_1 \rangle + \alpha_2 \langle N_2 \rangle \right)^2} \\ B_3 &= \frac{\langle N_1 \rangle + \alpha_2^3 \langle N_2 \rangle}{\left(\langle N_1 \rangle + \alpha_2 \langle N_2 \rangle \right)^3} \\ B_4 &= \frac{\langle N_1 \rangle + \alpha_2^4 \langle N_2 \rangle}{\left(\langle N_1 \rangle + \alpha_2 \langle N_2 \rangle \right)^4} \end{aligned} \tag{6}$$

It is important to note that Eq. (4) and (5) simply express $g_{n,m}$ (0,0) in terms of number density of predetermined constituent species (i.e., R), but do not determine which species it includes up to, i.e., up to trimer ($R = 3$) or up to tetramer ($R = 4$). This can be identified by the image intensity histogram. For low concentrations, it is expected that monomer and dimer numbers dominate other aggregates, hence it is reasonable to assume two species ($R = 2$).

In applying HICS to images of AuNPs, various emission modes, such as scattering, luminescence or even harmonic generations can be utilised. For DFM images, scattering is used as the emission process, therefore α_2 is interpreted as scattering cross-section ratio of the dimer to monomer. Dimers of 80 nm AuNPs show increase in total scattering intensity (integrated at 400–700 nm) between 2 to 4 times that of a monomer, depending on the gap distance between the nanoparticles in the dimer (calculated using finite element method, data not shown).

Biomedical Optics EXPRESS

2.2. Simulation of HICS

First, the validity of HICS was checked by analyzing simulated DFM images of randomly distributed AuNPs. Previously, Sergeev et al [63] extensively simulated and tested the validity of HICS for bimodal distribution of emissive species, i.e., monomer/dimer or monomer/ octamer, etc., and found that HICS is only accurate when the aggregate concentration is far lower than that of monomer, i.e., 2 orders of magnitude difference, $N_1 >> N_n$. Here, we demonstrate an improvement in the validity range of HICS. Our estimation shows that it is accurate up to comparable concentrations of monomer and oligomer, but loses accuracy when aggregate concentration is simply higher than that of monomer, i.e., $N_1 < N_n$. We also pay close attention to the relative concentration where HICS is deemed inaccurate, which has not been properly studied before.

Methodologically, we take a similar approach to the previous work by Sergeev et al [63], i.e., bimodal distribution of monomers and dimers, but take into account the different properties of the 80 nm diameter AuNP dimers. DFM simulation images for randomly positioned particles have Gaussian spots with radius of 5 pixels in a 256×256 pixels image size. For dimers the mean α_2 was 4 with a variable Gaussian spread with variance σ^2, between 0 and 4 was allowed. Gaussian random noise was added on each pixel as a background. Figure 1(a), (b), and (c) show typical simulated DFM images for varying concentrations of N_1 and N_2. The particular images were simulated with α_2 value being 4 ± 0.2. Further details are shown in the Methods section in the Supplemental document.

The HICS analyzed values of average monomers N_1 and dimers N_2 and α_2 from 200 simulated images are extracted using Eq. (3) to 5, and are plotted as points against the input values (lines) in Fig. 1(d), (e) and (f) for different N_2 concentrations, 0.001, 0.01 and 0.1, respectively. Gaussian noise background up to 50% of the monomer intensity could be successfully subtracted using the method by Petersen et al. [55] without affecting the extracted values of N_1, N_2 and α_2 (see Methods section in the Supplemental document for more details of noise correction). More on the signal to background noise ratio (SNR) and the particle size is discussed below. Gaussian variation of α_2 up to ± 2 did not affect the results. Beyond these points however, results were heavily distorted. In each plot in Fig. 1(d), (e) and (f), N_1 is varied between 0.001 to 10. It is clear from the figures, input and output values match almost perfectly for $N_1 \geq N_2$. Such a good agreement is a marked improvement from the previous data [63], and could be attributed to an improved algorithm used in extracting the solutions from nonlinear simultaneous equations of Eq. (6). We utilized commercial numerical package (NSolve function in Mathematica 12, Wolfram) to extract the solutions.

However, for the case where $N_1 < N_2$, output values fail to match the input lines (marked by grey area in Fig. 1(e) and 1(f)). In particular, N_1 is overestimated by almost 1 order of magnitude and N_2 is underestimated by half. Such deviation could be understood from the fact that high-order correlation function $g_{n,m}$ (0,0) is dominated by the oligomer contribution because of the factor α_2^m (m is the order of the image, ie., $m = 2, 3, 4 \ldots$, Eq. (6)), which makes the contribution from monomer concentration N_1 insignificant and error-prone when $N_1 < N_2$. In this region, two strategies can be taken to extract the concentration information. First, HICS can identify the dominant species concentration (N_2 in this case) as N_1 in the limit $N_1 << N_2$, because the contribution from monomer is insignificant. This means that the monomer concentration extracted can simply be interpreted as the dimer species. This can be seen in Fig. 1(e) and 1(f), that the N_1 points (black squares) tend towards N_2 input (red line) as $N_1 \rightarrow 0$. Simulation over 200 images in each data point showed that more than 80% of the time N_1 correctly extracted dimer concentrations. Second, $g_{1,1}$ (0,0) (or conventionally referred to as $g(0)$ in ICS) can be an alternative measure of the dominant dimer concentration N_2, as the correlation function is inundated by their contribution. This is represented as the green line and green square points ($N_p = 1/\, g(0)$), which tend towards the N_2 input (red line) as $N_1 \rightarrow 0$. Both methods extract the

Biomedical Optics EXPRESS

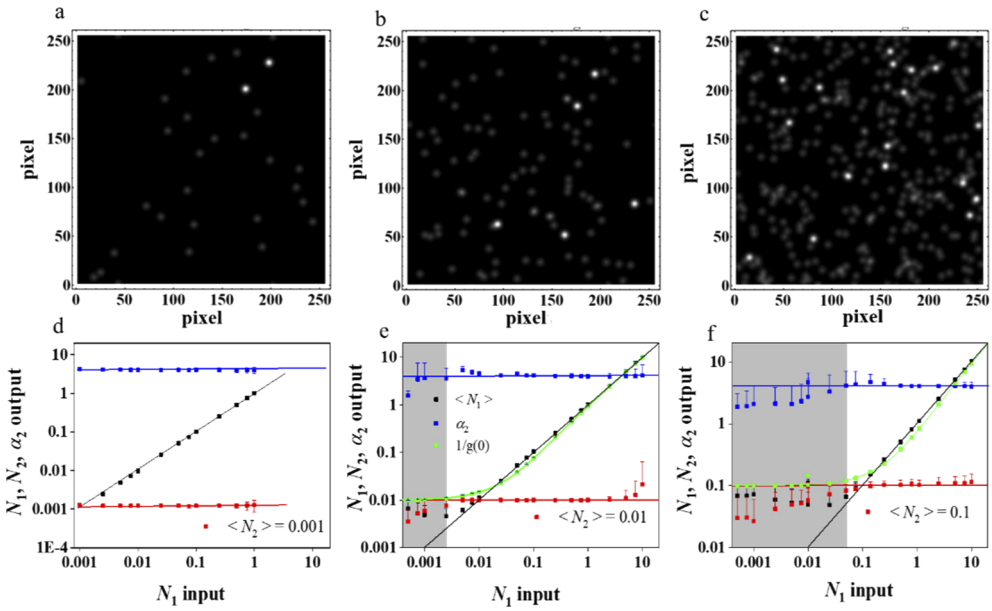

Fig. 1. Typical examples of simulated DFM images (a, b, and c) of randomly distributed 80 nm AuNPs at different monomer and dimer concentrations. All concentration values are in particles / beam area. (a) DFM image with $N_1 = 0.02$, $N_2 = 0.001$, (b) $N_1 = 0.1$, $N_2 = 0.01$, (c) $N_1 = 0.5$, $N_2 = 0.1$. All three images are 256×256 pixels in size with Gaussian focal spots at 5 pixels radius, background noise level of 0.01 of monomer intensity and $\alpha_2 = 4 \pm 0.2$. HICS analysis results (d, e, and f) for simulated images at different concentrations. In each plot, we fixed N_2 and varied N_1, between 0.001 to 10. (d) HICS analysis for $N_2 = 0.001$, (e) $N_2 = 0.01$, and (f) $N_2 = 0.1$, Input parameters are shown in lines, and extracted data are shown as points. Monomer N_1 are black squares, N_2 are red squares, α_2 are blue squares, and N_p extracted from $g_{1,1}(0,0)$ (i.e., $N_p, = 1/g(0) = 1/g_{1,1}(0,0)$) are shown as the green squares. Each point in the plot is an average from 200 simulated images, and error bars are standard deviation of the 200 simulations. Grey area shows the region where $N_1 < N_2$, in which the accuracy of HICS decreases. In this case, $N_p = 1/g_{1,1}(0,0)$ is a better measure of dominant dimer concentration, as can be seen that green squares match the red line (see text for the details).

Biomedical Optics EXPRESS

dominant species concentration at the cost of neglecting the monomer species concentration. We shall use such method in estimating the total uptake of particles in HeLa cells in section 4, where the concentration of dimers frequently overtakes that of monomers. This bimodal simulation results demonstrate that HICS analysis can be an accurate measure of particle concentration on either situations of concentration limits (i,e., $N_1 < N_2$ or $N_1 > N_2$).

The results shown in Fig. 1 apply to any size of particle provided the scattering SNR is high. In reality, as the particle size gets smaller, the signal strength decreases hence the SNR. Generally, scattering cross section of a sphere increases to sixth power of particle diameter ($\sim d^6$) up to 80 nm particles [65]. If the SNR is ~ 20 of the signal from monomer of 80 nm and this is assumed to be constant, then the minimum signal required is 10% of the signal of 80 nm monomer (assuming lowest detectable SNR is 2). The minimum diameter of particle d_{min} that will be detectable then is $d_{min} = d_{ref}\left(\frac{2}{SNR}\right)^{\frac{1}{6}}$ where d_{ref} is the reference particle diameter (80 nm in this case). This is equal to 54.5 nm. If the SNR increases to 100, the detectable size also reduces to 41.6 nm. Typical CCD camera SNR varies between $10 \sim 20$, therefore it is reasonable to limit the detectable size to 54.5 nm. However, this could be improved using enhanced detectors.

3. Experimental validation of HICS on random AuNPs

We further validate the accuracy of HICS analysis for randomly distributed low-concentration AuNPs on a coverslip glass for a non-cellular environment similar to the simulated images in Section 2. We use spectrum counting method to manually count the particles and compare the results to the HICS analysis to validate the method. The spectrum identification of nanoparticle dimers and aggregates is a well-established technique in DFM. Sonnichsen et al [66] used dimer scattering spectrum and intensity change to differentiate them to monomers, and Wang et al also showed the spectral shift of aggregates for their identification inside cells [32]. This is a useful method to cross-check the aggregate numbers but is not a replacement for HICS because of the low throughput of its procedure.

Briefly, AuNPs of 80 nm diameter coated with cetyltrimethylammonium bromide (CTAB) were purchased from NanoSeedz Ltd (NS-80-50, Hong Kong). AuNPs were diluted, then drop-cast and spincoated on a coverslip glass. We used commercial dark-field microscopy (Nikon Eclipse Ti-S and Nikon DS-Filc colour CCD camera) for imaging and a coupled spectrometer (SpectraPro 300i, Acton Research) for scattering spectroscopy. We selected a square region where only monomers and dimers are present for the HICS analysis. Once the images were taken, noise was subtracted and filtered for the HICS processing. Monomer and dimer spot numbers in the images were counted manually using the spectrum counting method. These are easily identified in the image due to their monomodal scattering intensity and distinct colours (SPR peak at 550 nm for monomer, $600 \sim 700$ nm for dimer). Monomer number dominated the image (~ 80% of the spots), and the rest of the spots were identified as aggregates. Dimers have their total intensity between two to four times that of monomers (i.e., $2 < \alpha_2 < 4$) with yellow to red colour. Details of the procedures are shown in Methods section in the Supplemental document.

Figure 2(a) shows a typical DFM image of randomly distributed 80 nm AuNPs where green particles are identified as monomers and orange-red spots are identified as dimers or aggregates. Figure 2(b) and (c) illustrate typical scattering spectrum of a monomer (b) and a dimer (c) measured by the spectrograph. Matching theory curves are overlaid, Mie Theory [67] for monomer and finite element method (FEM, COMSOL Multiphysics) simulation for the dimer with a gap of 7 nm in air (polarization in dimer axis). Scanning electron microscopy (SEM) images of a monomer and a dimer from the sample are also shown in the inset. The red-shift of plasmon peak is observed for dimers due to plasmon coupling [68]. Good agreement between theory and experiment is seen for both cases. In addition, dimers show an increase in the total scattering intensity, between $2 \sim 4$ times that of a monomer. Based on the spectrum measurement,

Biomedical Optics EXPRESS

monomer and dimer number could be counted from the image (spectrum counting method). Counting histogram of monomers and dimers from SEM images of larger area is shown in Fig. 2(d), which shows ~ 20% of dimer number to that of monomer. This matched well with the spectrum counting method.

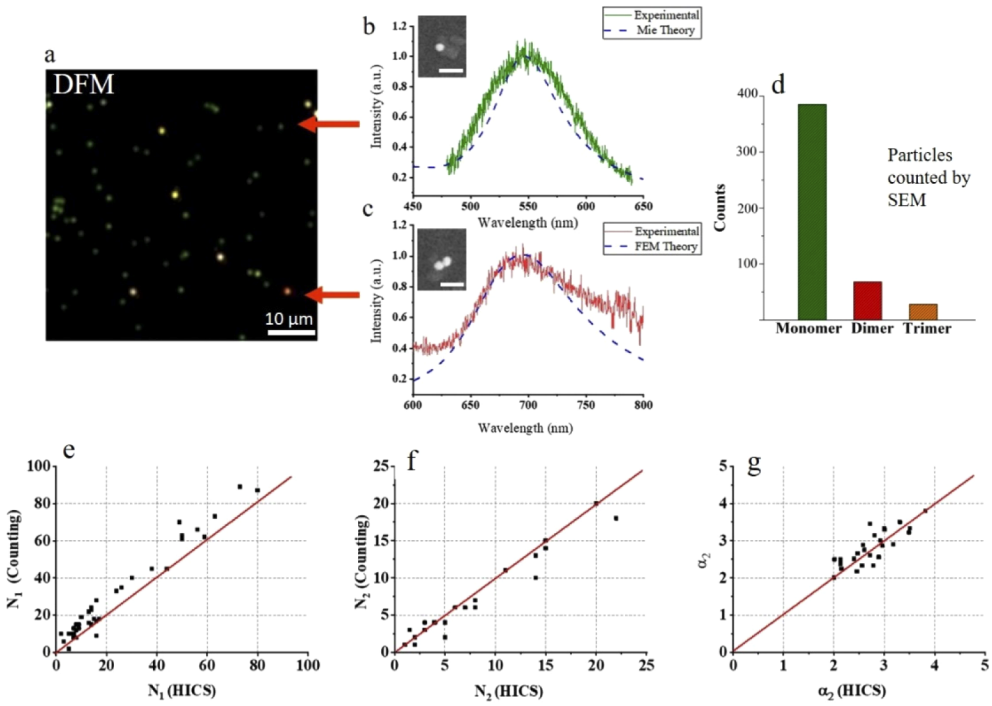

Fig. 2. (a) Typical DFM image of randomly distributed 80 nm AuNPs on a coverslip glass, forming monomers and dimers. (b) Scattering spectrum of a green (monomer) spot and matching Mie theory plot for a 80 nm AuNP in air. Inset shows an SEM image of a monomer with the scale bar 200 nm (c) Scattering spectrum of a red (dimer) spot and matching finite element method (FEM) numerical simulation of two 80 nm AuNPs separated by 7 nm gap. Inset shows an SEM image of a dimer with scale bar 200 nm. (d) Counted particles from SEM images. The ratio of the number of dimers to monomers is ~ 20%. Comparison between HICS analysis and spectrum counting method of total 50 images for (e) monomer number (N_1), (f) dimer number (N_2) and (g) scattering ratio dimer/monomer α_2 in the images. The red line is a guide to the eye for matching spectrum counting method to HICS analysis. Left (right) side of the red line means HICS analysis is underestimating (overestimating) the counting result.

We performed HICS analysis on the DFM images and compared with the spectrum counting method. Figure 2(e), (f) and (g) show the comparison for monomer, dimer number and α_2 from 50 DFM images. These numbers are all translated from N_1, N_2 and α_2 extracted by HICS, and the spectrum counting method. The figures show reasonable agreement between the two methods. Typical DFM images had N_1 on the order of 0.01 (particles per beam area), and N_2 on the order of 0.001 (particles per beam area), which correspond to simulation ranges for $N_1 > N_2$ in Fig. 1(d), where the accuracy of HICS is high. Some underestimation of N_1 by HICS analysis in Fig. 2(e) (i.e., left side of the red line) is attributed to the monomer intensity variation, which tends to reduce the particle number estimation as the variation increases [69]. In order to see the effect of varying the α_2, which incorporates monomer and dimer intensity variations caused by size distribution, a HICS analysis was conducted on simulated images created with a Gaussian

Biomedical Optics EXPRESS

distribution of α_2 with mean value at 3 and standard deviation of 1 (containing most of the dimer cross section variation within 2 to 4). The number variation was less than 1% for N_1, around 10% for α_2 and around 20% for N_2.

4. HICS analysis on the cellular uptake of AuNPs

After successful simulation and experimental validation, HICS analysis is extended to study cellular uptake of AuNPs in HeLa cells. Since destructive techniques (ICP-MS, ICP-AES) can only be used for ensemble averaging of cells in which single cell uptake information is buried, it is not ideal to use these techniques for correlated comparison. Instead we use spectrum counting method to build histogram of dimers and monomers on selected cells and use it to support the HICS analysis.

Briefly, HeLa cells (human cervical carcinoma) were cultured in a microslide chamber, and then a diluted solution of 80 nm spherical AuNPs coated with CTAB (NS-80-50, NanoSeedz Ltd) was diluted and added to the cultured HeLa cells and incubated for desired amount of time (0.5, 2, 4, 6, 8, 10, 24, and 48 hours), before fixing and washing. CTAB is cationic (ζ-potential ~ +40 mV), therefore are favorably taken up by negatively charged HeLa cell membrane [45]. Confocal laser scattering microscopy (CLSM) was used to check the particle internalization (See Fig. S1 in the Supplemental document for the details). DFM, described in section 3 was used to image the cells with AuNPs for the HICS analysis. Full details of the cell preparation are provided in the Methods section in the Supplemental document.

Figure 3 shows selected DFM images of AuNPs incubated in HeLa cells for different incubation times. It is clear that more particles are internalized into the cells as the incubation time increases. Higher-order aggregates of AuNPs could be observed in the cells, especially for longer hours of the uptake process. While HICS can be extended to identifying these aggregate species, in practice it requires a higher dynamic range and SNR of the image detectors because the quantum yield ratios $\boldsymbol{\alpha}_{\mathrm{i}}$ for aggregates vary wildly, for example between 3 ~ 9 for trimers, and even higher range for tetramers or pentamers. A high dynamic range generally reduces the SNR for monomers because to accommodate a high intensity variation, monomer signal enhancement must be sacrificed. For our case of using CCD detectors, optimizing the SNR meant that any aggregate signals higher than dimers were removed from the HICS analysis. Perhaps a point detection confocal microscopy approach using avalanche photodiodes with a dynamic range of ~ 10^6 could accommodate the wide variation in intensity while keeping the SNR high.

To gauge relative concentrations of monomers and dimers inside the cells, hence be able to determine which high-order correlation functions to use in extracting parameters, we again utilized the spectrum counting method to count monomers and dimer numbers in 5 randomly selected cell images and built histograms for each incubation time. This is shown in Fig. 4. It can be seen that up to 6 hours of incubation, monomer number is larger than dimer number in the images, i.e, $\boldsymbol{N}_1 > \boldsymbol{N}_2$. As shown by our simulations in section 2.2, for this relative concentration of monomers and dimers, HICS can be used to extract $\boldsymbol{N}_1$, $\boldsymbol{N}_2$, and $\boldsymbol{\alpha}_2$ with accuracy level of maximum 10% error. Beyond 6 hours, however, dimer number is larger than monomer i.e, $\boldsymbol{N}_1 < \boldsymbol{N}_2$. In this case, $1/g_{1,1}$ (0,0) is a better indicator of the dominant species number, dimers. We shall therefore take the $g_{1,1}$ (0,0) values in estimating the total number of dimers. The variation of $\boldsymbol{\alpha}_2$ in the histogram is between 1.7 and 2.5 depending on the hours, and the background noise level is less than 10% of the monomer intensity, which are within the allowed limit for HICS analysis.

The actual HICS analysis on 25 DFM cell images per data point is shown in Fig. 5. In Fig. 5(a), average monomer and dimer numbers in cells, and in Fig. 5(b), $\boldsymbol{\alpha}_2$ with respect to incubation time up to 6 hours are shown. It is interesting to note that as the incubation time increases, number of dimers increase while the number of monomers peaks at 4 hours and then stay steady. $\boldsymbol{\alpha}_2$ stays consistently within 2.6–2.7 range, which means that the coupling distance is ~ 20 nm (FEM

Biomedical Optics EXPRESS

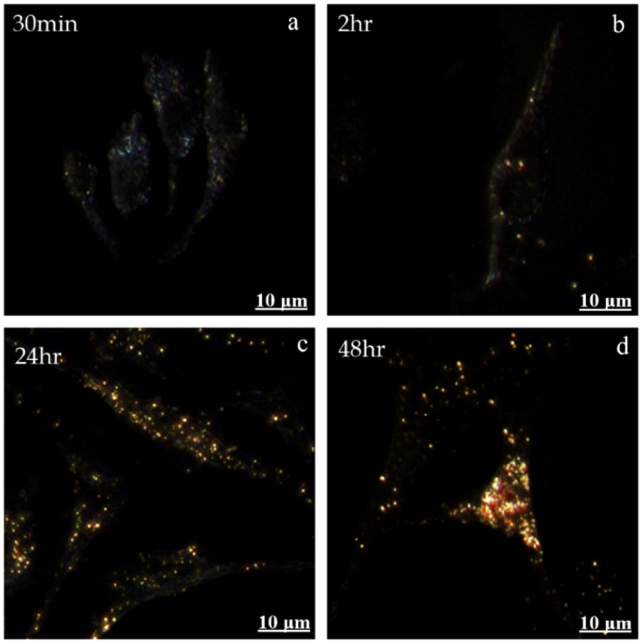

Fig. 3. Dark-field scattering images for 80 nm AuNPs for different incubation times, (a) 30 mins, (b) 2 hours, (c) 24 hours and (d) 48 hours. As the incubation time increases the nanoparticle cellular uptake increases.

simulation). These numbers match reasonably well with the histogram in Fig. 4 and demonstrate the utility of HICS analysis.

In Fig. 5(c) beyond 8 hours of incubation, $g_{1,1}$ (0,0) values are extracted from 25 images (instead of $g_{n,m}$ (0,0) for the reason discussed above), and used it to estimate the total number of dominant species, dimers. It shows that the uptake is more or less saturated beyond 10 hours. Overall number of AuNPs are estimated from these analyses and plotted in Fig. 5(d), where the increase in uptake happens mostly in the first 10 hours, and then stay steady up to 48 hours. The large variation in total number of uptake particles per cell (Fig. 5(d)) demonstrates that individual cells behave differently in uptake of particles, which could be due to different uptake kinetics, different nanoparticle capacity or a combination of both.

The uptake half-life was measured to be 6 hours, with the uptake rate of ~ 17 particles per hour. The average number of particles at steady-state was ~ 250 at 48 hours. As a point of reference Chithrani et al. previously reported, for 74 nm citrate coated AuNPs at concentration of 0.02 nM, uptake half-life of 2.24 hours at the uptake rate 417 particles per hour [34,35]. The maximum uptake reported was ~ 2988 particles per cell. Wang et al. reported 70 nm AuNPs coated with ssDNA, with a maximum uptake of ~ 128 particles per cell [37]. Since the experimental conditions of these reports were not identical to our current study it is impossible to directly compare these values to the current results. Differences between the reports are in fact real, and a reflection of actual differences in size and concentration of the particles [34], and ligand molecules [45]. Lower uptake half-life and slower uptake rate observed in our experiment are attributed to much lower concentration in our solution (~ 0.0076 nM), but the cationic nanoparticles (CTAB coating) improves the uptake. The saturation pattern of the uptake kinetics is nevertheless consistent with the literature report [34,35].

The current study reveals the percentage of dimerization of AuNPs during the uptake. It is clear that dimers are present at the early stages of uptake (30 mins) and the percentage of it increases

Biomedical Optics EXPRESS

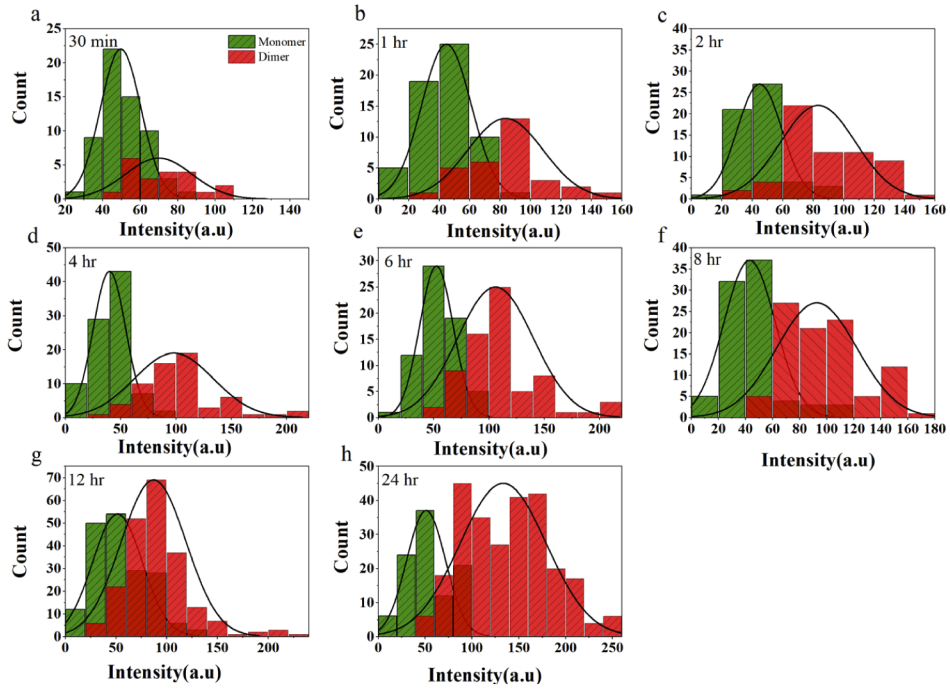

Fig. 4. Histogram of peak intensity counts from individual spots of 80 nm AuNPs inside 5 randomly selected cells. These histograms are constructed from spectrum counting method. (a) 30 mins (b) 1 hour (c) 2 hours (d) 4 hours (e) 6 hours (f) 8 hours (g) 12 hours (h) 24 hours. Green bars represent monomers and red bars for dimers. Note the number of dimers increases as the incubation time increases, but monomer numbers saturate at 4 ~ 6 hours.

from 25% (30 mins) to nearly 100% (48 hour) indicating that dimerization or oligomerization become more prevalent form of nanoparticles within the cells as the incubation time increases. Receptor-mediated endocytosis producing vesicles that contain aggregates of AuNPs are reported previously [35] and simulation showed cooperative uptake process by forming aggregates [70]. However, the percentage increase in dimers or aggregates with respect to incubation time has not been reported previously and it may indicate that simple charge-driven uptake could also drive the aggregation of particles inside the cells in an effort to maximize the uptake. Further studies in size, functionalization and concentration will be needed to understand the observation. Such details of uptake are not easily observed in other methods and the current HICS methodology is clearly advantageous.

Biomedical Optics EXPRESS

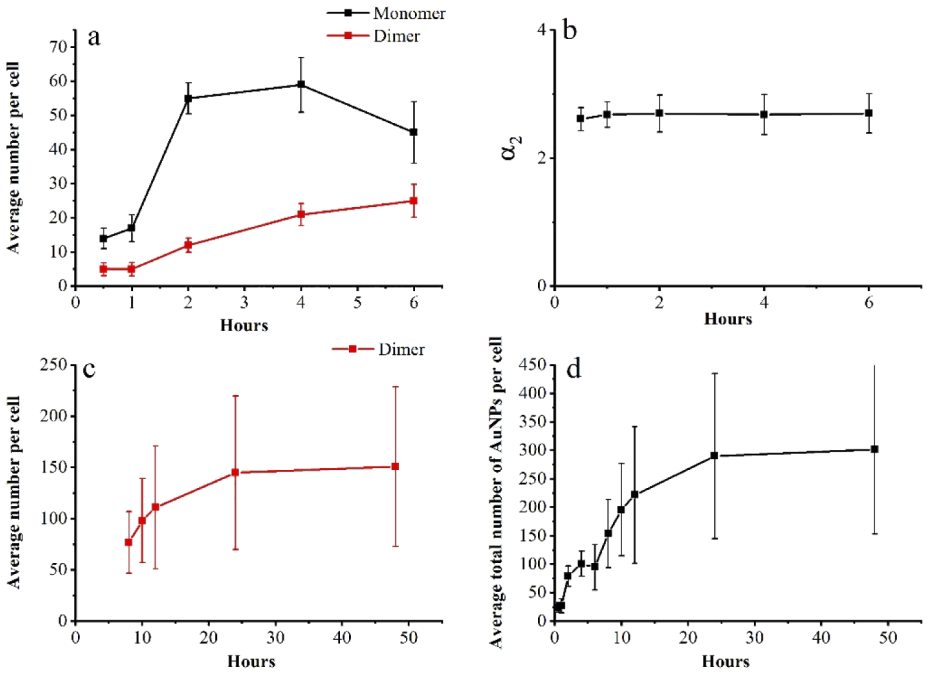

Fig. 5. The cellular uptake and aggregation of 80 nm AuNPs as the function of incubation time. All data points are average for 25 DFM cell images, with standard deviation shown as error bars. (a) HICS extracted total number of monomers and dimers per cell, showing flattening in monomer species after 4 hours, while dimers continue to increase up to 48 hours. (b) HICS extracted α_2 showing consistently ~ 2.5, (c) Total number of dimers is extracted by using $g_{1,1}$ (0,0) in the concentration regime where $N_1 < N_2$, and (d) Total number of AuNPs in the cells, calculated from (a) and (c). The total number up to 6 hours is the number of monomers plus the number of dimers from (a), and from 8 hours it is 2 x number of dimers from (c). Large variation per cell shows that individual cells behave differently in uptake, where some cells do not uptake much whereas some cells are maximally loaded with particles.

5. Conclusions

A new uptake quantification method based on non-destructive optical intensity high-order moment analysis is proposed and demonstrated. We validated the HICS methodology for computer simulated DFM images of AuNPs and identified a suitable range of relative aggregate species concentration for HICS validity. Generally, if monomeric species dominate aggregate species, HICS can be used with high accuracy, but if aggregate species dominate the monomeric species, $g_{1,1}$ (0,0) value can be taken to calculate the dominant aggregate species concentration. HICS is then further validated experimentally in non-cellular environment, where a good agreement in spectrum counting method and HICS method was observed. Finally, HICS was applied and demonstrated to DFM images of CTAB coated 80 nm AuNPs in HeLa cells, incubated for various hours up to 48 hours, showing a similar uptake trend of overall number of particles. More specifically, extra information such as percentage of dimerization in incubation, or the aggregate quantum yield ratio could be extracted, which was previously not possible with the destructive methods. Increase in percentage of dimers with respect to incubation hours indicate that oligomerization and aggregation is a preferred form over monomeric form, while the cell is driving its uptake to its maximum.

Biomedical Optics EXPRESS

While the HICS method is demonstrated for monodispersed spherical particles, its extension into different shapes for the particles, such as nanorods, could form an important future work, as more anisotropic particles become used as drug delivery agents. Their variation in coupling geometries will cause a large distribution in α_2, and since the current form of HICS does not incorporate a variation in quantum yield this would require a different formulation to the current form. Petersen previously applied a distribution of quantum yield to the theory of ICS [69] and so this could be incorporated into HICS theory in the future. This would be highly beneficial in counting multiple nanoparticle population and their numbers inside cells.

Funding. Australian Research Council.

Acknowledgments. Authors would like to thank A. S. M. Mohsin, Timothy T. Y. Chow, and Chiara Paviolo for useful discussions.

Disclosures. The authors declare no conflicts of interest.

See Supplement 1 for supporting content containing Methods section and CLSM images of HeLa cells loaded with AuNPs.

References

1. A. R. Rastinehad, H. Anastos, E. Wajswol, J. S. Winoker, J. P. Sfakianos, S. K. Doppalapudi, M. R. Carrick, C. J. Knauer, B. Taouli, S. C. Lewis, A. K. Tewari, J. A. Schwartz, S. E. Canfield, A. K. George, J. L. West, and N. J. Halas, "Gold nanoshell-localized photothermal ablation of prostate tumors in a clinical pilot device study," Proc. Natl. Acad. Sci. U. S. A. **116**(37), 18590–18596 (2019).
2. S. Jain, D. G. Hirst, and J. M. O'Sullivan, "Gold nanoparticles as novel agents for cancer therapy," Br. J. Radiol. **85**(1010), 101–113 (2012).
3. E. B. Dickerson, E. C. Dreaden, X. Huang, I. H. El-Sayed, H. Chu, S. Pushpanketh, J. F. McDonald, and M. A. El-Sayed, "Gold nanorod assisted near-infrared plasmonic photothermal therapy (PPTT) of squamous cell carcinoma in mice," Cancer Lett. **269**(1), 57–66 (2008).
4. L. Gao, J. Fei, J. Zhao, H. Li, Y. Cui, and J. Li, "Hypocrellin-loaded gold nanocages with high two-photon efficiency for photothermal/photodynamic cancer therapy in vitro," ACS Nano **6**(9), 8030–8040 (2012).
5. E. D. Onal and K. Guven, "Plasmonic photothermal therapy in third and fourth biological windows," J. Phys. Chem. C **121**(1), 684–690 (2017).
6. L. R. James, Z. Q. Xu, R. Sluyter, E. L. Hawksworth, C. Kelso, B. Lai, D. J. Paterson, M. D. de Jonge, N. E. Dixon, J. L. Beck, S. F. Ralph, and C. T. Dillon, "An investigation into the interactions of gold nanoparticles and anti-arthritic drugs with macrophages, and their reactivity towards thioredoxin reductase," J. Inorg. Biochem. **142**, 28–38 (2015).
7. M. Kodiha, Y. M. Wang, E. Hutter, D. Maysinger, and U. Stochaj, "Off to the organelles - killing cancer cells with targeted gold nanoparticles," Theranostics **5**(4), 357–370 (2015).
8. Y. Wang, J. Chen, and J. Irudayaraj, "Nuclear targeting dynamics of gold nanoclusters for enhanced therapy of HER2+ breast cancer," ACS Nano **5**(12), 9718–9725 (2011).
9. L. R. Hirsch, R. J. Stafford, J. A. Bankson, S. R. Sershen, B. Rivera, R. E. Price, J. D. Hazle, N. J. Halas, and J. L. West, "Nanoshell-mediated near-infrared thermal therapy of tumors under magnetic resonance guidance," Proc. Natl. Acad. Sci. U. S. A. **100**(23), 13549–13554 (2003).
10. X. Huang, I. H. El-Sayed, W. Qian, and M. A. El-Sayed, "Cancer cell imaging and photothermal therapy in the near-infrared region by using gold nanorods," J. Am. Chem. Soc. **128**(6), 2115–2120 (2006).
11. W. Kim, K. Y. Na, K. H. Lee, H. W. Lee, J. K. Lee, and K. T. Kim, "Selective uptake of epidermal growth factor-conjugated gold nanoparticle (EGF-GNP) facilitates non-thermal plasma (NTP)-mediated cell death," Sci. Rep. **7**(1), 10971 (2017).
12. C. Paviolo, J. W. Chon, and A. H. Clayton, "Inhibiting EGFR clustering and cell proliferation with gold nanoparticles," Small **11**(14), 1638–1643 (2015).
13. L. A. Dykman and N. G. Khlebtsov, "Multifunctional gold-based nanocomposites for theranostics," Biomaterials **108**, 13–34 (2016).
14. C. C. Huang and T. M. Liu, "Controlled Au-polymer nanostructures for multiphoton imaging, prodrug delivery, and chemo-photothermal therapy platforms," ACS Appl. Mater. Interfaces **7**(45), 25259–25269 (2015).
15. Z. Zhang, L. Wang, J. Wang, X. Jiang, X. Li, Z. Hu, Y. Ji, X. Wu, and C. Chen, "Mesoporous silica-coated gold nanorods as a light-mediated multifunctional theranostic platform for cancer treatment," Adv. Mater. **24**(11), 1418–1423 (2012).
16. X. Wang, X. Qian, J. J. Beitler, Z. G. Chen, F. R. Khuri, M. M. Lewis, H. J. Shin, S. Nie, and D. M. Shin, "Detection of circulating tumor cells in human peripheral blood using surface-enhanced Raman scattering nanoparticles," Cancer Res. **71**(5), 1526–1532 (2011).
17. H. Deng, F. Dai, G. Ma, and X. Zhang, "Theranostic gold nanomicelles made from biocompatible comb-like polymers for thermochemotherapy and multifunctional imaging with rapid clearance," Adv. Mater. **27**(24), 3645–3653 (2015).

Biomedical Optics EXPRESS

18. J. Yue, T. J. Feliciano, W. Li, A. Lee, and T. W. Odom, "Gold nanoparticle size and shape effects on cellular uptake and intracellular distribution of siRNA nanoconstructs," Bioconjug. Chem. **28**(6), 1791–1800 (2017).
19. S. Sindhwani, A. M. Syed, J. Ngai, B. R. Kingston, L. Maiorino, J. Rothschild, P. MacMillan, Y. Zhang, N. U. Rajesh, T. Hoang, J. L. Y. Wu, S. Wilhelm, A. Zilman, S. Gadde, A. Sulaiman, B. Ouyang, Z. Lin, L. Wang, M. Egeblad, and W. C. W. Chan, "The entry of nanoparticles into solid tumours," Nat. Mater. **19**(5), 566–575 (2020).
20. V. Voliani, F. Ricci, G. Signore, R. Nifosi, S. Luin, and F. Beltram, "Multiphoton molecular photorelease in click-chemistry-functionalized gold nanoparticles," Small **7**(23), 3271–3275 (2011).
21. S. Kumar, J. Aaron, and K. Sokolov, "Directional conjugation of antibodies to nanoparticles for synthesis of multiplexed optical contrast agents with both delivery and targeting moieties," Nat. Protoc. **3**(2), 314–320 (2008).
22. J. Aaron, K. Travis, N. Harrison, and K. Sokolov, "Dynamic imaging of molecular assemblies in live cells based on nanoparticle plasmon resonance coupling," Nano Lett. **9**(10), 3612–3618 (2009).
23. W. Jiang, B. Y. Kim, J. T. Rutka, and W. C. Chan, "Nanoparticle-mediated cellular response is size-dependent," Nat. Nanotechnol. **3**(3), 145–150 (2008).
24. P. Falagan-Lotsch, E. M. Grzincic, and C. J. Murphy, "One low-dose exposure of gold nanoparticles induces long-term changes in human cells," Proc. Natl. Acad. Sci. U. S. A. **113**(47), 13318–13323 (2016).
25. N. Gunduz, H. Ceylan, M. O. Guler, and A. B. Tekinay, "Intracellular accumulation of gold nanoparticles leads to inhibition of macropinocytosis to reduce the endoplasmic reticulum stress," Sci. Rep. **7**(1), 40493 (2017).
26. G. Bodelón, C. Costas, J. Pérez-Juste, I. Pastoriza-Santos, and L. M. Liz-Marzán, "Gold nanoparticles for regulation of cell function and behavior," Nano Today **13**, 40–60 (2017).
27. Y. Wu, M. R. K. Ali, K. Chen, N. Fang, and M. A. El-Sayed, "Gold nanoparticles in biological optical imaging," Nano Today **24**, 120–140 (2019).
28. J. Comenge, O. Fragueiro, J. Sharkey, A. Taylor, M. Held, N. C. Burton, B. K. Park, B. Wilm, P. Murray, M. Brust, and R. Levy, "Preventing plasmon coupling between gold nanorods improves the sensitivity of photoacoustic detection of labeled stem cells in vivo," ACS Nano **10**(7), 7106–7116 (2016).
29. N. J. Durr, T. Larson, D. K. Smith, B. A. Korgel, K. Sokolov, and A. Ben-Yakar, "Two-photon luminescence imaging of cancer cells using molecularly targeted gold nanorods," Nano Lett. **7**(4), 941–945 (2007).
30. N. Li, M.-M. Jie, M. Yang, L. Tang, S.-Y. Chen, X.-M. Sun, B. Tang, and S.-M. Yang, "Magnetic gold nanoparticle-labeled heparanase monoclonal antibody and its subsequent application for tumor magnetic resonance imaging," Nanoscale Res. Lett. **13**(1), 106 (2018).
31. S. Lee, H. Chon, M. Lee, J. Choo, S. Y. Shin, Y. H. Lee, S. W. Son, and C. H. Oh, "Surface-enhanced Raman scattering imaging of HER2 cancer markers overexpressed in single MCF7 cells using antibody conjugated hollow gold nanospheres," Biosens. Bioelectron. **24**(7), 2260–2263 (2009).
32. H. Wang, G. Rong, B. Yan, L. Yang, and B. M. Reinhard, "Optical sizing of immunolabel clusters through multispectral plasmon coupling microscopy," Nano Lett. **11**(2), 498–504 (2011).
33. L. A. Dykman and N. G. Khlebtsov, "Immunological properties of gold nanoparticles," Chem. Sci. **8**(3), 1719–1735 (2017).
34. B. D. Chithrani, A. A. Ghazani, and W. C. Chan, "Determining the size and shape dependence of gold nanoparticle uptake into mammalian cells," Nano Lett. **6**(4), 662–668 (2006).
35. B. D. Chithrani and W. C. Chan, "Elucidating the mechanism of cellular uptake and removal of protein-coated gold nanoparticles of different sizes and shapes," Nano Lett. **7**(6), 1542–1550 (2007).
36. A. Albanese and W. C. Chan, "Effect of gold nanoparticle aggregation on cell uptake and toxicity," ACS Nano **5**(7), 5478–5489 (2011).
37. S. H. Wang, C. W. Lee, A. Chiou, and P. K. Wei, "Size-dependent endocytosis of gold nanoparticles studied by three-dimensional mapping of plasmonic scattering images," J. Nanobiotechnol. **8**(1), 33 (2010).
38. N. Oh and J. H. Park, "Surface chemistry of gold nanoparticles mediates their exocytosis in macrophages," ACS Nano **8**(6), 6232–6241 (2014).
39. C. Rosman, S. Pierrat, A. Henkel, M. Tarantola, D. Schneider, E. Sunnick, A. Janshoff, and C. Sonnichsen, "A new approach to assess gold nanoparticle uptake by mammalian cells: combining optical dark-field and transmission electron microscopy," Small **8**(23), 3683–3690 (2012).
40. L. A. Dykman and N. G. Khlebtsov, "Uptake of engineered gold nanoparticles into mammalian cells," Chem. Rev. **114**(2), 1258–1288 (2014).
41. H. Klingberg, L. B. Oddershede, K. Loeschner, E. H. Larsen, S. Loft, and P. Møller, "Uptake of gold nanoparticles in primary human endothelial cells," Toxicol. Res. **4**(3), 655–666 (2015).
42. G. Zhou, N. Liu, Z. Wang, T. Shi, J. Gan, Z. Wang, and J. Zhang, "Quantitative analysis of gold and carbon nanoparticles in mammalian cells by flow cytometry light scattering," J. Nanopart. Res. **19**(2), 78 (2017).
43. A. Buonerba, R. Lapenta, A. Donniacuo, M. Licasale, E. Vezzoli, S. Milione, C. Capacchione, M. F. Tecce, A. Falqui, R. Piacentini, C. Grassi, and A. Grassi, "NIR multiphoton ablation of cancer cells, fluorescence quenching and cellular uptake of dansyl-glutathione-coated gold nanoparticles," Sci. Rep. **10**(1), 11380 (2020).
44. M. Matczuk, L. Ruzik, S. S. Aleksenko, B. K. Keppler, M. Jarosz, and A. R. Timerbaev, "Analytical methodology for studying cellular uptake, processing and localization of gold nanoparticles," Anal. Chim. Acta **1052**, 1–9 (2019).
45. J. Mosquera, M. Henriksen-Lacey, I. Garcia, M. Martinez-Calvo, J. Rodriguez, J. L. Mascarenas, and L. M. Liz-Marzan, "Cellular uptake of gold nanoparticles triggered by host-guest interactions," J. Am. Chem. Soc. **140**(13), 4469–4472 (2018).

Biomedical Optics EXPRESS

46. C. Kinnear, T. L. Moore, L. Rodriguez-Lorenzo, B. Rothen-Rutishauser, and A. Petri-Fink, "Form follows function: nanoparticle shape and its implications for nanomedicine," Chem. Rev. **117**(17), 11476–11521 (2017).
47. T. D. Rane and A. M. Armani, "Two-photon microscopy analysis of gold nanoparticle uptake in 3D cell spheroids," PLoS One **11**(12), e0167548 (2016).
48. K. Nambara, K. Niikura, H. Mitomo, T. Ninomiya, C. Takeuchi, J. Wei, Y. Matsuo, and K. Ijiro, "Reverse size dependences of the cellular uptake of triangular and spherical gold nanoparticles," Langmuir **32**(47), 12559–12567 (2016).
49. R. Xu, B. Xiong, R. Zhou, H. Shen, E. S. Yeung, and Y. He, "Pericellular matrix plays an active role in retention and cellular uptake of large-sized nanoparticles," Anal. Bioanal. Chem. **406**(20), 5031–5037 (2014).
50. J.-H. Park, J. Park, U. Dembereldorj, K. Cho, K. Lee, S. I. Yang, S. Y. Lee, and S.-W. Joo, "Raman detection of localized transferrin-coated gold nanoparticles inside a single cell," Anal. Bioanal. Chem. **401**(5), 1631–1639 (2011).
51. L. Wang, Y.-F. Li, L. Zhou, Y. Liu, L. Meng, K. Zhang, X. Wu, L. Zhang, B. Li, and C. Chen, "Characterization of gold nanorods in vivo by integrated analytical techniques: their uptake, retention, and chemical forms," Anal. Bioanal. Chem. **396**(3), 1105–1114 (2010).
52. A. Malugin and H. Ghandehari, "Cellular uptake and toxicity of gold nanoparticles in prostate cancer cells: a comparative study of rods and spheres," J. Appl. Toxicol. **30**(3), n/a (2009).
53. D. L. Kolin and P. W. Wiseman, "Advances in image correlation spectroscopy: measuring number densities, aggregation states, and dynamics of fluorescently labeled macromolecules in cells," Cell Biochem. Biophys. **49**(3), 141–164 (2007).
54. N. O. Petersen, P. L. Hoddelius, P. W. Wiseman, O. Seger, and K. E. Magnusson, "Quantitation of membrane receptor distributions by image correlation spectroscopy: concept and application," Biophys. J. **65**(3), 1135–1146 (1993).
55. N. O. Petersen, C. Brown, A. Kaminski, J. Rocheleau, M. Srivastava, and P. W. Wiseman, "Analysis of membrane protein cluster densities and sizes in situ by image correlation spectroscopy," Faraday Discuss. **111**, 289–305 (1999).
56. P. Wiseman, J. Squier, M. Ellisman, and K. Wilson, "Two-photon image correlation spectroscopy and image cross-correlation spectroscopy," J. Microsc. **200**(1), 14–25 (2000).
57. B. Hebert, S. Costantino, and P. W. Wiseman, "Spatiotemporal image correlation spectroscopy (STICS) theory, verification, and application to protein velocity mapping in living CHO cells," Biophys. J. **88**(5), 3601–3614 (2005).
58. G. D. Ciccotosto, N. Kozer, T. T. Chow, J. W. Chon, and A. H. Clayton, "Aggregation distributions on cells determined by photobleaching image correlation spectroscopy," Biophys. J. **104**(5), 1056–1064 (2013).
59. C. Paviolo, J. W. M. Chon, and A. H. A. Clayton, "The effect of nanoparticles on the cluster size distributions of activated EGFR measured with photobleaching image correlation spectroscopy," Adv. Exp. Med. Biol **1112**, 41–52 (2018).
60. M. A. Digman, P. Sengupta, P. W. Wiseman, C. M. Brown, A. R. Horwitz, and E. Gratton, "Fluctuation correlation spectroscopy with a laser-scanning microscope: exploiting the hidden time structure," Biophys. J. **88**(5), L33–L36 (2005).
61. A. G. Palmer 3rd and N. L. Thompson, "Molecular aggregation characterized by high order autocorrelation in fluorescence correlation spectroscopy," Biophys. J. **52**(2), 257–270 (1987).
62. A. G. Palmer 3rd and N. L. Thompson, "High-order fluorescence fluctuation analysis of model protein clusters," Proc. Natl. Acad. Sci. U. S. A. **86**(16), 6148–6152 (1989).
63. M. Sergeev, S. Costantino, and P. W. Wiseman, "Measurement of monomer-oligomer distributions via fluorescence moment image analysis," Biophys. J. **91**(10), 3884–3896 (2006).
64. M. Sergeev, J. L. Swift, A. G. Godin, and P. W. Wiseman, "Ligand-induced clustering of EGF receptors: a quantitative study by fluorescence image moment analysis," Biophys. Chem. **161**, 50–53 (2012).
65. A. Tcherniak, J. W. Ha, S. Dominguez-Medina, L. S. Slaughter, and S. Link, "Probing a century old prediction one plasmonic particle at a time," Nano Lett. **10**(4), 1398–1404 (2010).
66. C. Sönnichsen, B. M. Reinhard, J. Liphardt, and A. P. Alivisatos, "A molecular ruler based on plasmon coupling of single gold and silver nanoparticles," Nat. Biotechnol. **23**(6), 741–745 (2005).
67. G. Mie, "Beiträge zur Optik trüber Medien, speziell kolloidaler Metallösungen," Ann. Phys. **330**(3), 377–445 (1908).
68. J. M. McMahon, A. I. Henry, K. L. Wustholz, M. J. Natan, R. G. Freeman, R. P. Van Duyne, and G. C. Schatz, "Gold nanoparticle dimer plasmonics: finite element method calculations of the electromagnetic enhancement to surface-enhanced Raman spectroscopy," Anal. Bioanal. Chem. **394**(7), 1819–1825 (2009).
69. N. O. Petersen, "Scanning fluorescence correlation spectroscopy. I. Theory and simulation of aggregation measurements," Biophys. J. **49**(4), 809–815 (1986).
70. B. J. Reynwar, G. Illya, V. A. Harmandaris, M. M. Müller, K. Kremer, and M. Deserno, "Aggregation and vesiculation of membrane proteins by curvature-mediated interactions," Nature **447**(7143), 461–464 (2007).